Nawaz et al. *Microsystems & Nanoengineering* (2026)12:104
https://doi.org/10.1038/s41378-025-01137-5

Microsystems & Nanoengineering
www.nature.com/micronano

ARTICLE Open Access

Advanced reusable SAW-based particulate matter sensor with microheater and porous microstructured filter membrane for simultaneous PM10 and PM2.5 detection

Faisal Nawaz[1], Nuriddin Tavakkalov[1] and Keekeun Lee[1,2]✉

Abstract

In this study, we present a novel reusable surface acoustic wave (SAW)-based particulate matter (PM) sensor system capable of simultaneously and selectively detecting PM10 and PM2.5. This is the first implementation of an integrated porous microstructure membrane, acting as a mechanical filter for particle separation, combined with an on-board microheater for particle detachment, enabling sensor reusability. The membrane featured holes of approximately 3 µm and 11 µm in diameter, allowing for selective detection of PM2.5 and PM10, respectively. A two-port SAW resonator structure and 128° YX $LiNbO_3$ substrate was selected for the sensor platform. The microheater was co-fabricated with the SAW sensor to reduce additional processing time and cost. The porous membrane filter was placed over the sensor, covering only the interdigital transducers (IDTs) and reflectors. COMSOL simulations were used to analyze the heater's thermal performance, particle trajectories, and eventual particle detachment following microheater activation. For experiments, highly sensitive and stable multi-channel interface electronics were developed to monitor real-time frequency shifts. Sensors were tested in a vacuum chamber with manually controlled particle inlet and microheater. Testing was conducted using PM10 and PM2.5 fine dust, and the sensor demonstrated high sensitivity to both PM categories. A detailed calibration study was performed to ensure the system exclusively detects PM10 and PM2.5. After exposing the sensor surface to three different concentrations of PM, the microheater was activated by applying 12 V, allowing the device to reach a maximum temperature of approximately 100 °C. This facilitated the sensor's recovery to baseline levels under vacuum conditions, making the sensor reusable.

Introduction

Particulate matter (PM) is recognized as one of the most critical environmental pollutants, posing significant risks to both human health and the environment[1–3]. It consists of various harmful substances, including organic salts, inorganic metal oxides, inorganic carbon, soot, and fly ash, and its concentration in the atmosphere continues to rise over time due to anthropogenic and natural sources[4,5]. PM is typically classified into three categories based on particle size: PM10 (particles with a diameter ≤10 µm), PM2.5 (≤2.5 µm), PM1.0 particles (≤1.0 µm) and ultrafine particles (UFPs, ≤0.1 µm)[6]. Due to their diminutive size, PM2.5 particles bypass the bronchial mucosa, directly entering the lungs and thereby jeopardizing human health[7,8]. These particles are linked to severe respiratory and cardiovascular diseases and are a leading cause of morbidity and mortality worldwide[9]. Additionally, PM contributes to environmental degradation, manifesting in reduced visibility, acid rain, and disruptions to cloud formation, which collectively impact natural ecosystems[10]. Studies suggest that PM2.5 can act as a vector for airborne viruses, including the SARS-CoV-2 virus, increasing the risk of infection and mortality[9]. Recognizing its detrimental health impacts, the World Health

Correspondence: Keekeun Lee (keekeun@ajou.ac.kr)
[1]Department of Electrical and Computer Engineering, Ajou University, Suwon 16499, Republic of Korea
[2]Department of Intelligence Semiconductor Engineering, Ajou University, Suwon 16499, Republic of Korea

Organization (WHO) classified PM as a Group 1 carcinogen in 2013. A study reported that a 10 μg/m^3 increase in PM10 concentration heightened the relative risk of mortality, cardiovascular disease, ischemic heart disease, heart failure, and stroke mortality by 24%, 23%, 37%, 11%, and 23%, 37%, 11%, and 23%, respectively[11,12]. Research has demonstrated that a 10 μg/m^3 increase in PM2.5 concentration could elevate the COVID-19 fatality rate by 8%[13].

Several methods are currently used to measure PM, with the main techniques being beta ray absorption[14], gravimetric collection[15], and light scattering[16]. Beta ray absorption measures the intensity of beta rays absorbed as they pass through collected particulate matter. The system consists of a fine dust intake, a dust classifier, tape filters, a beta ray source, and a detector. While this method offers high accuracy and a low minimum detection limit, it requires bulky dust classifiers and relies on an X-ray source and detector, which can present challenges in terms of stability, portability, and cost[17,18]. Gravimetric collection involves capturing fine dust on a filter and calculating mass concentration based on the weight difference before and after collection. The fine dust particles are collected through an impactor, and the weight is measured. However, chemical reactions can lead to the formation of solid-phase salts, which can either overestimate or underestimate the mass concentration, leading to measurement errors. Gravimetric collection relies on filter weighing and is prone to errors caused by chemical reactions such as salt formation or water uptake[19,20]. In contrast, the SAW sensor detects particles through real-time frequency shifts without any weighing step. This acoustic principle is well established as a reliable, non-gravimetric, mass-sensitive technique[21]. Light scattering directs light at particles passing through a measurement space, causing the light to scatter[16]. The scattered light is detected by a photodetector, generating an electrical signal proportional to the amount of particulate matter. However, light scattering methods tend to be less precise because factors like particle density, shape, and humidity can influence results[22]. At high PM concentrations, multiple light scattering, diffraction, and deflection can occur before the light reaches the detector, leading to accuracy issues[23].

Particulate matter classifiers commonly include cascade impactors[24], cyclones[25], and mechanical filters[26], each utilizing different physical principles to separate particles based on size or mass. Among these, the impactor is the most commonly used type. It typically consists of several single-stage impactors arranged in series to form a cascade impactor structure. Impactors separate particles by mass using inertial force; however, they have several limitations, including particle bounce, re-entrainment, overloading, and particle loss[27]. A cyclone uses centrifugal force to separate particles by mass, where heavier particles are carried by the swirling flow and collected, while lighter particles are separated by the reversing flow due to the interaction between centrifugal and drag forces[28]. A mechanical filter classifies particles based on hole size, distinguishing PM10, PM2.5, and PM1.0[29]. It requires a large open area, high mechanical strength, and minimal particle absorption onto the filter walls during penetration.

In recent years, surface acoustic wave (SAW)-based sensors have gained significant attention for particulate matter detection[30,31]. Operating at high frequencies, SAW sensors are highly sensitive to mass loading, offering superior sensitivity compared to traditional quartz crystal microbalance devices[32,33]. Additionally, the acoustic energy in SAW sensors is concentrated near the surface, further enhancing their sensitivity to particulate matter[34,35]. However, existing studies on SAW-based PM sensors have primarily focused on those that employ direct particle attachment mechanisms, which often result in irreversible particle binding and limited reusability. Additionally, many of these studies did not address the separation of PM10 and PM2.5 particles. For instance, some SAW-based PM sensors relied on single-use particle attachment approaches[21,36]. Similarly, our previous study demonstrated effective PM sensing but did not explore particle separation or the recovery process[37]. While these approaches demonstrated high sensitivity, their lack of reusability limited their practical applicability.

In this study, we introduce, for the first time, a novel SAW PM sensor system featuring a porous microstructure filter membrane (mechanical filter), along with an integrated microheater and temperature sensor. The porous membrane effectively differentiates between PM10 and PM2.5 by employing size-selective filters with pore sizes of 11 μm for PM10 and 3 μm for PM2.5, respectively. This design offers a cost-effective and reliable alternative to conventional separators, such as impactors and cyclones, which often lack particle selectivity. Furthermore, unlike conventional SAW PM sensors that typically lack recovery mechanisms, our design incorporates a built-in microheater and temperature sensor. The sensor surface is equipped with a microheater that generates high heat to evaporate particles attached to the surface, allowing the sensor to be reused. Additionally, the use of interface electronics minimizes environmental interference, such as temperature variation and vibration, thereby improving measurement accuracy.

Results and discussion

Device description and sensing principle

Figure 1a illustrates the overall developed SAW PM sensor system, which includes microporous filter membranes of 11 μm and 3 μm mounted above two sensors

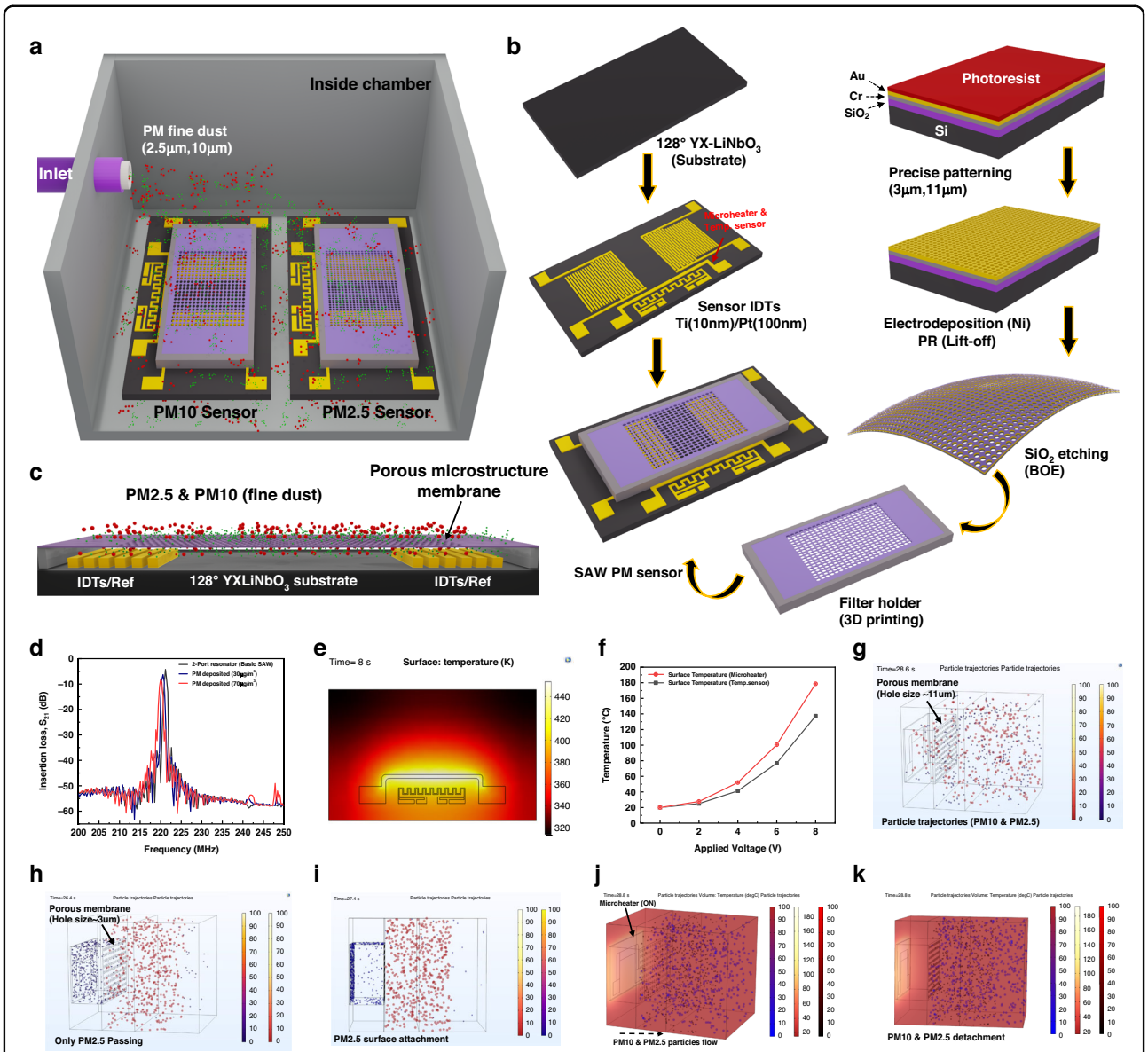

Fig. 1 Overview, fabrication, and simulation of the developed SAW-based PM sensor system. a Structural view of the SAW PM sensors inside the chamber. **b** Overall view of the PM10 sensor, showing both particles (PM10 and PM2.5) passing through the membrane and depositing on the sensor surface. **c** Overall fabrication process of the SAW PM sensor. **d** COM modeling result showing the frequency response (S_{21}) of the two-port SAW resonator before and after when PM is attached. **e** Simulated heat distribution on the sensor surface using an in-plane microheater, showing the maximum temperature within the targeted heating area. **f** Relationship between the applied voltage and surface temperature measured at the cavity deposition area, where PM particles are expected to attach. **g** PM10 and PM2.5 particles passing through an 11 μm filter and attaching to the sensor surface. **h** Only PM2.5 particles pass through a 3 μm filter, while PM10 particles are blocked. **i** Vertical cross-sectional view of the 3 μm filter, clearly showing selective passage of PM2.5. **j** Localized heating from the embedded microheater initiates the removal of particles from the sensor surface. **k** Vertical perspective illustrating the particle detachment process during and after heating

operating at a 222 MHz center frequency for PM10 and PM2.5 detection. The porous membranes selectively allow the passage of target fine dust particles based on their size and are positioned above each sensor. Both sensors are placed inside the chamber (Fig. 1a), where fine dust particles are introduced. A microheater is integrated into the sensor surface to enable the desorption of particulate matter from both the sensor and membrane surfaces by applying sufficient heat, thereby allowing the sensor to be reused. The integrated microheater promotes particle desorption by providing localized thermal energy, which overcomes adhesion forces and restores the sensor baseline, consistent with temperature-programmed desorption studies in SAW sensors and related microheater-

based systems[38–40]. The complete fabrication process is presented in Fig. 1b. An overall view of the PM10 sensor with the integrated 11 μm porous membrane is shown in Fig. 1c, where both PM10 and PM2.5 particles pass through the membrane and reach the sensor surface. As PM passes through the porous membrane and adheres to the sensor surface, a shift in the center frequency of the SAW sensor occurs due to the mass loading effect. In contrast, the reference SAW device remains unaffected, as it is enclosed by a 3D-printed frame without a window, preventing particle deposition. To maximize detection sensitivity, the porous membrane filter was positioned directly above the cavity between the two IDTs, ensuring that dust particles primarily settle in this region—where the SAW sensor exhibits the greatest velocity and frequency response to mass changes. The overall operating mechanism for frequency shift measurement and PC-based display with environmental compensation is shown in Fig. S1. The frequency difference between the sensing and reference devices (fr−fs) effectively compensates for environmental interference such as temperature and vibration (Fig. S1). For the sensing mechanism of PM detection using a SAW sensor, the frequency shift behavior caused by particle attachment was discussed in detail in our previous study[37]; therefore, a full explanation is omitted here. Based on that work and supporting literature, it was found that to achieve effective acoustic coupling with an entire particle, the penetration depth of the SAW wave should approximately match the diameter of a PM2.5 particle. Accordingly, a center frequency of 222 MHz was selected, as it provides an appropriate penetration depth for sensing PM2.5. Although PM10 particles are significantly larger and would generally require a lower frequency to achieve full coupling, we used the same 222 MHz frequency for both PM2.5 and PM10 configurations. This approach was chosen to maintain consistency in the sensing setup and enable a direct, controlled comparison of the microfilter structures. Importantly, even though the penetration depth is smaller than the full PM10 diameter, Rayleigh waves remain sensitive to surface loading effects, and our calibration procedure effectively resolves the PM2.5 and PM2.5–PM10 fractions.

Device design and simulations

A coupling-of-modes (COM) analysis was performed to optimize the SAW sensor design. The objective was to minimize insertion loss at the center frequency while achieving high sidelobe levels in the S_{21} response. Key modifications included reducing the number of IDT pairs, optimizing the reflector number, adjusting the aperture, and employing a nominal cavity size. These measures minimized device size while reducing insertion loss. A two-port SAW resonator operating at 222 MHz on a 128° YX $LiNbO_3$ substrate was selected, owing to its high SAW velocity and strong electromechanical coupling coefficient (K^2). The optimized design achieved an insertion loss of ~4.1 dB at the center frequency, which is significantly lower than previously reported studies[41–43]. We selected a Rayleigh-mode SAW resonator on 128° YX $LiNbO_3$ to enable seamless integration of the porous membrane and on-chip microheater; unlike Love/SH devices that require an optimized wave-guiding layer (increasing insertion loss and complicating thermal cycling)[34,35]. In air, Rayleigh's strong surface-normal displacement and surface acoustic energy density produce larger phase-velocity perturbations from rigid particulates at the free surface, yielding higher practical SNR under PM loading. While $LiNbO_3$ also offers high electromechanical coupling ($k^2 \approx 5$–11%), our choice is driven by this combination of surface sensitivity, process simplicity, and robustness, which we leverage for linear, thermally regenerable PM sensing. The mass loading effect was also modeled to evaluate the frequency shift and insertion loss when particles were deposited on the surface. As shown in Fig. 1d, particle attachment increased insertion loss and downshifted the center frequency. The optimized parameters were used for device fabrication, and the measured results closely matched the simulations with only minor deviations. The modeling parameters are summarized in Table S1, and the detailed COM modeling procedure has been reported previously[41–43].

Two types of COMSOL simulations were performed to guide the device design: (i) microheater simulations, which optimized the heater geometry to achieve uniform surface heating at low input voltage, and (ii) filter membrane simulations, which evaluated pore size, thickness, and material to ensure selective permeability, efficient infiltration, and reliable particle desorption. A Pt-based microheater was modeled to deliver uniform thermal energy across the sensing area, with key parameters such as line geometry, resistivity ($\rho = 1.96 \times 10^{-8}$ Ω m), and cross-sectional area (~20 μm²) optimized to minimize power consumption while maintaining effective heat transfer. As shown in Fig. 1e, f, the device achieved uniform temperature distribution, with surface temperature rising proportionally under applied voltages up to 8 V, confirming consistent and efficient heating performance. The porous filter membrane was optimized to balance permeability, selectivity, and mechanical stability by systematically varying pore shape, open-area ratio, thickness, and material composition. Circular pores provided the best compromise between infiltration and robustness; thinner membranes enhanced diffusion but were more prone to deformation, whereas a slightly thicker Au-coated Ni membrane offered durability, reduced electrostatic adhesion, and improved dust permeability. Particle tracing simulations were then performed under

atmospheric conditions by introducing fine particles into the system. With an 11 µm membrane, both 10 µm and 2.5 µm particles passed through (Fig. 1g), whereas the 3 µm membrane selectively allowed only 2.5 µm particles while blocking 10 µm particles (Fig. 1h). A vertical cross-sectional view further illustrates this selective permeability (Fig. 1i). Finally, microheater-assisted regeneration was simulated to assess particle detachment: upon heating, particles detached from both the filter and sensor surfaces (Fig. 1j), and a vertical perspective of this process confirmed that thermal activation enables repeatable regeneration and long-term sensor reusability (Fig. 1k). Collectively, these simulations validate the complementary roles of the microheater and porous membrane in enabling selective particle filtration, efficient sensing, and reliable recovery.

Experimental setup and fabricated device

The PM measurement system, depicted in Fig. 2a, comprises a fine-dust tank, a test chamber, SAW sensors with integrated interface electronics, and a data acquisition setup. The fine-dust tank contains PM2.5 and PM10 particles (Sigma Aldrich) and uniformly disperses them into the test chamber through controlled airflow, regulated by a vacuum pump and pressure gauge. Inside the chamber, SAW sensors and a commercial PM sensor facilitate real-time monitoring. Reference SAW devices, fully covered with 3D frames without any pores, are also positioned inside the chamber. Before each test cycle, the test chamber is purged using a vacuum pump to establish a stable baseline on the sensor surface. PM2.5 particles were introduced first, followed by a PM10 mixture containing PM2.5 particles, with data recorded for each. A manually controlled microheater heated the sensor to 100 °C, based on the pre-measured and set values. After heating, the system cooled, allowing particle detachment and baseline recovery.

An optical view of the fabricated sensor is shown in Fig. 2b. The accompanying SEM image highlights the Pt IDTs and reflectors, with a finger width of 4.4 µm. Advanced interface electronics were developed to simultaneously measure and display frequency shifts from two SAW sensors on a PC. The system includes individual reference SAW devices for each sensor to compensate for environmental perturbations such as temperature and vibration. The interface electronics consist of two reference SAW devices, oscillators, mixers, low-pass filters (LPFs), comparators, a field-programmable gate array (FPGA), and a PC. To enhance portability, reduce noise, and achieve miniaturization, the mixer, LPF, and comparator were integrated into a single-chip interface, requiring only one chip per sensor and significantly simplifying the system configuration (Fig. 2c). The SAW devices were wire-bonded to oscillator pads to form a feedback loop comprising an RF amplifier (UPC2713T), a phase shifter, and the SAW sensor. Oscillator outputs were routed to an RF mixer (AD831), generating frequency components corresponding to the sum and difference of the input signals. An LPF with a 2 MHz cutoff frequency filtered out unwanted components, isolating the frequency difference signal (fr−fs). A comparator (LM393) then converted the filtered sine wave into a square wave, suitable for digital input to the FPGA (Xilinx Spartan-7, XC7S25-1CSGA225C). The FPGA processed the frequency data and transmitted it to the PC through a UART module using standard serial communication protocols. Real-time frequency difference signals of both sensors were displayed on the PC. The developed system exhibited a sensitivity of approximately 1 Hz, enabling the detection of minute variations.

Fabricated porous microstructure filter membrane

A porous membrane was fabricated to serve as a mechanical filter while addressing key challenges such as structural uniformity, mechanical stiffness, and surface roughness. These issues were resolved through process optimization prior to the final fabrication. Surface roughness was minimized by depositing an additional gold layer after membrane fabrication, while nickel was selectively deposited along the side regions without perforations to enhance handling and mechanical stability, resulting in straight, unbent edges. An overall optical view of the fabricated membrane is shown in Fig. 3ai, and its flatness and robustness are further demonstrated by handling with tweezers in Fig. 3aii. The elemental composition of the porous membrane, obtained by energy-dispersive X-ray spectroscopy (EDS), is presented in Fig. 3b, confirming the presence of Ni and Au. Nickel was used to provide structural support and thickness around the porous region, while gold was used both as a base and as a top coating to enhance smoothness, hydrophobicity, and particle passage. To assemble the membrane onto the sensor, a custom 3D-printed frame holder was fabricated, as illustrated in Fig. 3ci. An optical image of the holder is shown in Fig. 3cii, while Fig. 3ciii shows the membrane mounted onto the frame for alignment above the sensor surface. The key fabrication parameters of the 3D-printed holder are summarized in Fig. 3civ, including pixel size, lift speed, printing time, and holder dimensions. Fig. 3d shows the SEM images of the fabricated porous membrane filter. The overall top view of the membrane structure is presented in Fig. 3di, while higher-magnification images are shown in Fig. 3dii and Fig. 3diii, highlighting the regularity and uniformity of the pore pattern. Fig. 3div provides an edge view of the membrane, intentionally captured to demonstrate surface smoothness, assess membrane thickness, and visualize the

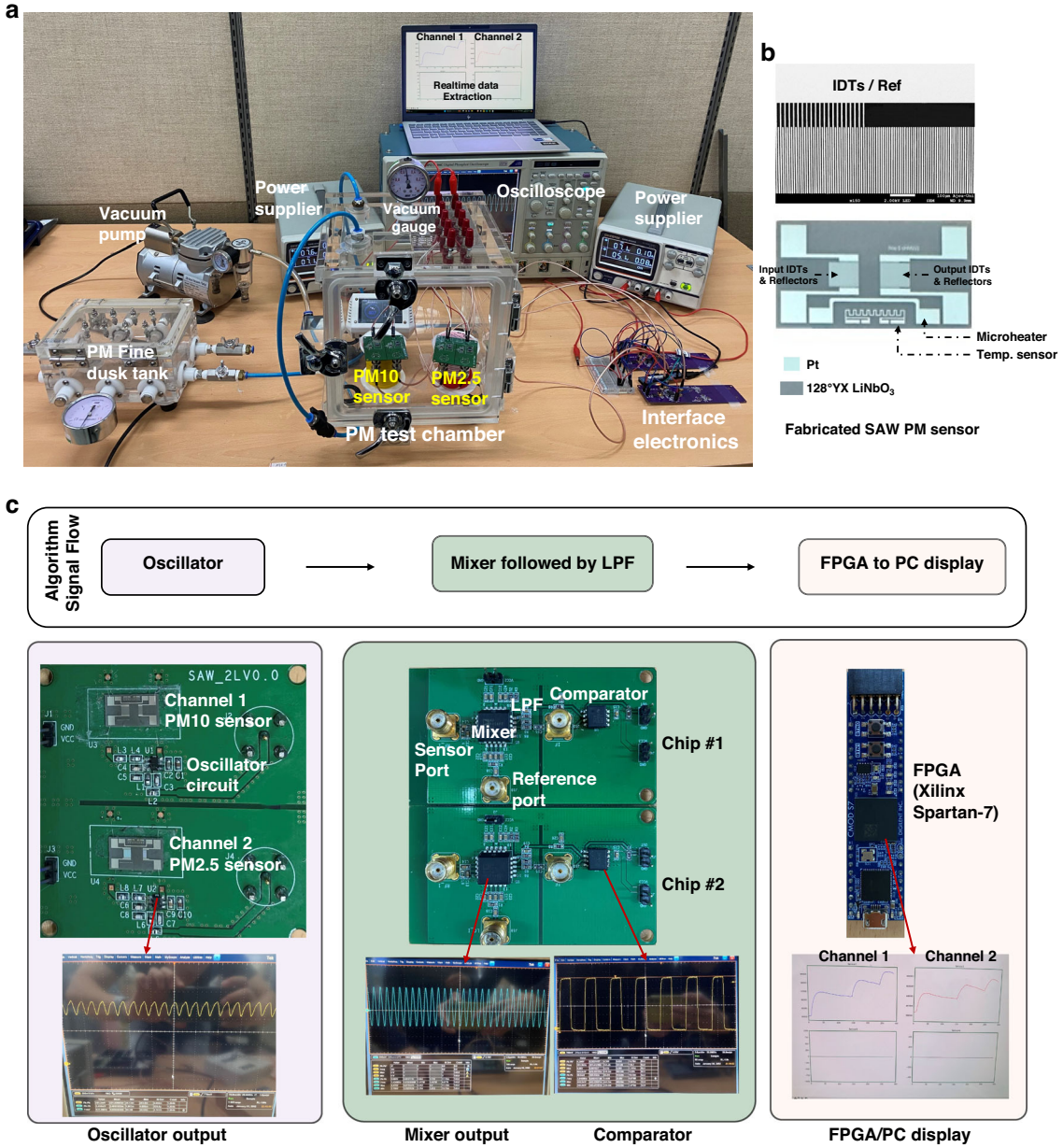

Fig. 2 Overview of the developed testing setup and fabricated device. a developed measurement system for PM detection, including a fine-dust tank, test chamber, vacuum pump, interface electronics, and data acquisition setup. **b** Optical view of the fabricated two-port SAW resonator on 128° YX-cut $LiNbO_3$ with integrated microheater and temperature sensor, alongside an SEM of the IDT array with reflector (scale bar: 100 µm). **c** View of the interface electronics components used to measure frequency shifts, showing signal outputs at key stages

pore geometry from a 3D perspective. A closer view of this area is presented in Fig. 3dv, revealing more detailed structural features. Fig. 3dvi shows a close-up of a single pore with a diameter of approximately 10.9 µm, confirming its suitability for PM10 detection. Fig. 3dvii highlights a smaller pore with a diameter of approximately 3.08 µm, confirming its effectiveness for selective PM2.5 filtration. Fig. 3dviii presents the cross-sectional view of the PM2.5 filter membrane, showing that a thickness of ~2 µm was deposited for the PM2.5 filter. The SEM analysis verifies the membrane's structural integrity, uniform pore distribution, and its capability for accurate particulate matter separation, which is essential for air quality monitoring. AFM analysis was performed to evaluate the surface morphology of the fabricated porous membranes. For a fair comparison, AFM scans were acquired over a 50 × 50 µm area for both samples, one without Au coating (Ni only) and one with Au coating on

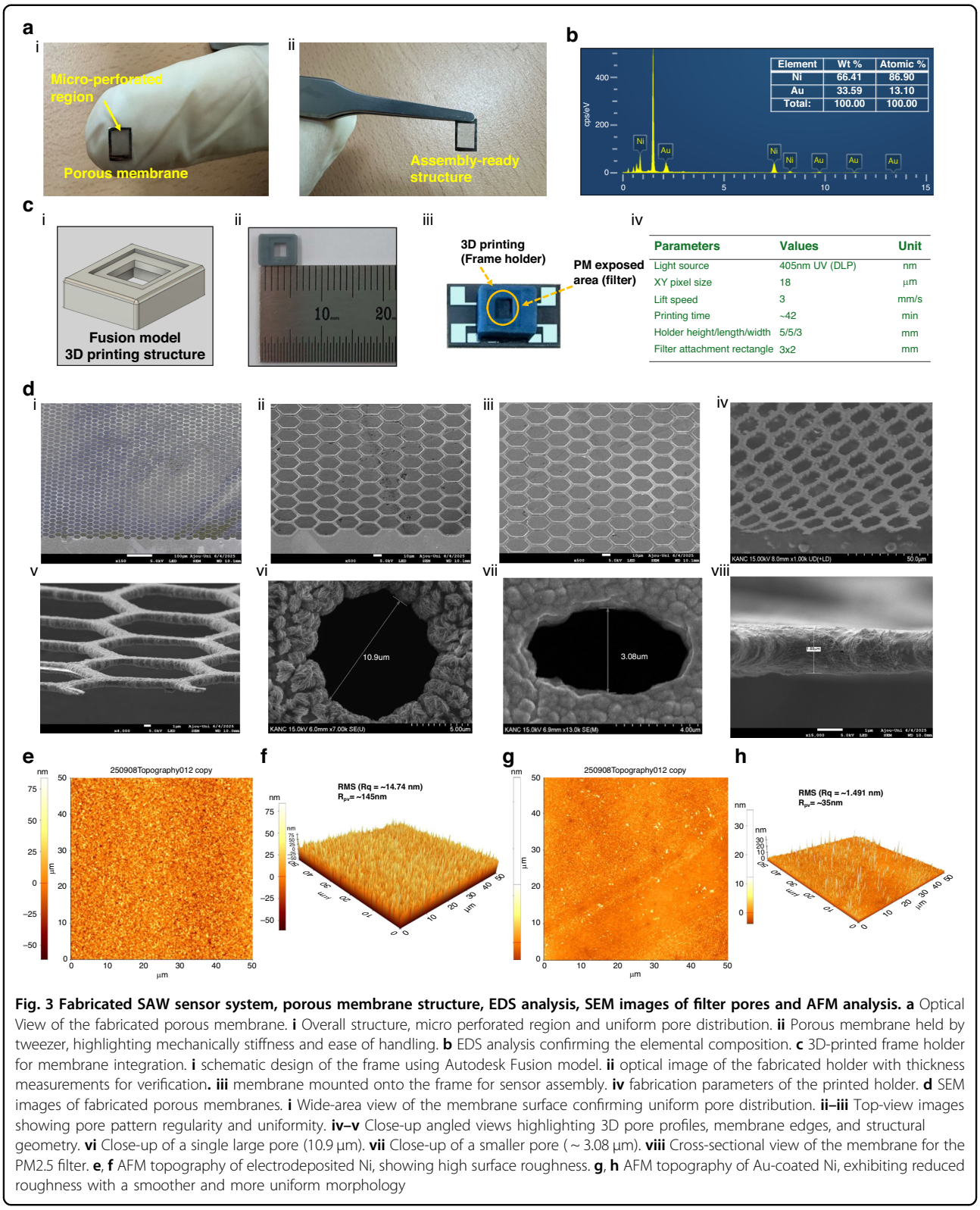

Fig. 3 Fabricated SAW sensor system, porous membrane structure, EDS analysis, SEM images of filter pores and AFM analysis. a Optical View of the fabricated porous membrane. **i** Overall structure, micro perforated region and uniform pore distribution. **ii** Porous membrane held by tweezer, highlighting mechanically stiffness and ease of handling. **b** EDS analysis confirming the elemental composition. **c** 3D-printed frame holder for membrane integration. **i** schematic design of the frame using Autodesk Fusion model. **ii** optical image of the fabricated holder with thickness measurements for verification**. iii** membrane mounted onto the frame for sensor assembly. **iv** fabrication parameters of the printed holder. **d** SEM images of fabricated porous membranes. **i** Wide-area view of the membrane surface confirming uniform pore distribution. **ii–iii** Top-view images showing pore pattern regularity and uniformity. **iv–v** Close-up angled views highlighting 3D pore profiles, membrane edges, and structural geometry. **vi** Close-up of a single large pore (10.9 μm). **vii** Close-up of a smaller pore (~ 3.08 μm). **viii** Cross-sectional view of the membrane for the PM2.5 filter. **e**, **f** AFM topography of electrodeposited Ni, showing high surface roughness. **g**, **h** AFM topography of Au-coated Ni, exhibiting reduced roughness with a smoother and more uniform morphology

Ni. Additional scans at different areas were also measured, but the representative results with the most uniform structures are presented here to support our conclusions.

As shown in Fig. 3e, f, the bare Ni membrane exhibited pronounced surface roughness, with an RMS roughness (Rq) of ~14.7 nm and a Rpv of ~145 nm, reflecting the

granular nature of electrodeposited Ni. In contrast, the Au-coated Ni membrane (Fig. 3g, h) demonstrated a much smoother morphology, with the RMS roughness reduced to ~1.5 nm and Rpv limited to ~35 nm. The Au/Ni surface effectively planarized the Ni asperities and provided a smoother morphology. Although occasional peak features were still visible, these were sparse and did not significantly affect the average roughness. Collectively, these results confirm that Au deposition improves structural uniformity, reduces electrostatic adhesion, and produces a stable surface morphology suitable for consistent sensor operation. To evaluate the mechanical robustness and ductility of the porous membrane, mechanical stress tests were conducted by bending, shaking, and pressing the detached filter. It was also exposed to air and humidity for an extended period. Despite these conditions, the membrane remained structurally intact and undamaged, attributed to its ductile mechanical properties and inert surface coating.

Characterization of SAW sensor using a network analyzer

Prior to conducting sensor measurements with the interface electronics, the fabricated sensor was initially characterized using a network analyzer to verify the resonant frequency and evaluate its consistency with analytical COM modeling. The sensor was wire-bonded to the PCB pads, and to minimize variations in resonant frequency and insertion loss due to parasitic capacitance, inductance, and resistance, the wire lengths were kept as short as possible. Fig. 4ai presents the S_{21} characteristics of the two-port SAW resonator sensor measured with the network analyzer. The device exhibited an insertion loss of −13.27 dB at a center frequency of 222.52 MHz, with a high sidelobe level and a stable, high-amplitude main lobe signal. The resonance peak at 222.52 MHz exhibits a 3 dB bandwidth of ~0.25 MHz, corresponding to a Q-factor of ~890.08, indicative of strong frequency selectivity and low acoustic loss, key features for highly sensitive detection. To further confirm the mass-loading response, PM deposition (250 μg/m²) was applied, and the resulting frequency shift was measured directly using the network analyzer. The results, shown in Fig. 4aii, revealed a clear, concentration-dependent frequency shift in good agreement with the COM modeling predictions. Since both sensors were fabricated identically, only one device was characterized with the network analyzer to confirm the baseline S_{21} response, mass loading, and frequency shifts. The subsequent real-time measurements, including PM2.5 and PM10 testing, were carried out using the developed interface electronics. This approach was chosen because the interface system allowed evaluation of parameters that could not be fully captured with a conventional network analyzer, such as response time, saturation behavior, real-time frequency display, microheater-assisted recovery, and clear differentiation between PM2.5 and PM10 signals.

PM sensor characterization using interface electronics

Experimental tests were conducted by placing PM10 (channel 1) and PM2.5 (channel 2) sensors inside a test chamber, each equipped with filter membranes having pore sizes of 11 μm and 3 μm, respectively. Both sensors were simultaneously exposed to PM particles, with the reference devices enclosed in a 3D-printed frame without any open areas, all placed inside the test chamber. The vacuum pump was activated to clean the test chamber before introducing the target particle concentration. The particle concentration inside the chamber was monitored using a commercially available PM sensor (MSMS-S4, Shanghai XuanHan Electronics Technology Co., Ltd.), which measures the total PM mass concentration in μg/m^3, regardless of particle size. Initially, PM2.5 particles (Sigma-Aldrich) were introduced into the test chamber, and both sensors responded accordingly. Three consecutive injections of particulate matter were performed, during which saturation behavior was observed. As shown in Fig. 4bi, the PM2.5 sensor (channel 2) exhibited frequency shifts of up to 6.9 kHz, while the PM10 sensor (channel 1) demonstrated shifts of up to 16.1 kHz when exposed to PM2.5 particles at a maximum concentration of 80 μg/m^3. The slightly greater frequency change observed in the PM10 sensor is attributed to the filter's larger hole size and open area. Even when the same atmospheric PM2.5 concentration (μg/m^3) is introduced to both sensors, differences in infiltration rates result in different frequency changes. Based on these results, the frequency responses of both sensors to PM2.5 particles were calibrated, as illustrated in Fig. 4bii. The evaluated sensitivity of the PM2.5 sensor to PM2.5 particles was 0.11 kHz/(μg/m^3), while the sensitivity of the PM10 sensor to PM2.5 particles was 0.246 kHz/μg/m^3. Subsequently, when PM10 particles were introduced into the chamber, both sensors responded, as PM10 particles inherently contain a fraction of PM2.5 particles. The PM10 sensor (channel 1) exhibited a maximum frequency shift of approximately 20.1 kHz, while the PM2.5 sensor showed a shift of up to ~4 kHz, as illustrated in Fig. 4biii. Since the PM10 sensor responds to both PM10 and PM2.5 particles, it was necessary to isolate the portion of its response specifically attributable to particles in the PM2.5 and PM10–PM2.5 size ranges. To achieve this, the concentration of PM2.5 particles inside the chamber was first determined using the PM2.5 sensor. Then, by subtracting the frequency shift caused by PM2.5 particles from the total frequency shift measured by the PM10 sensor, the contribution from particles in the PM2.5–PM10 range was isolated and used for calibration. This yielded the net frequency shift in the PM10 sensor

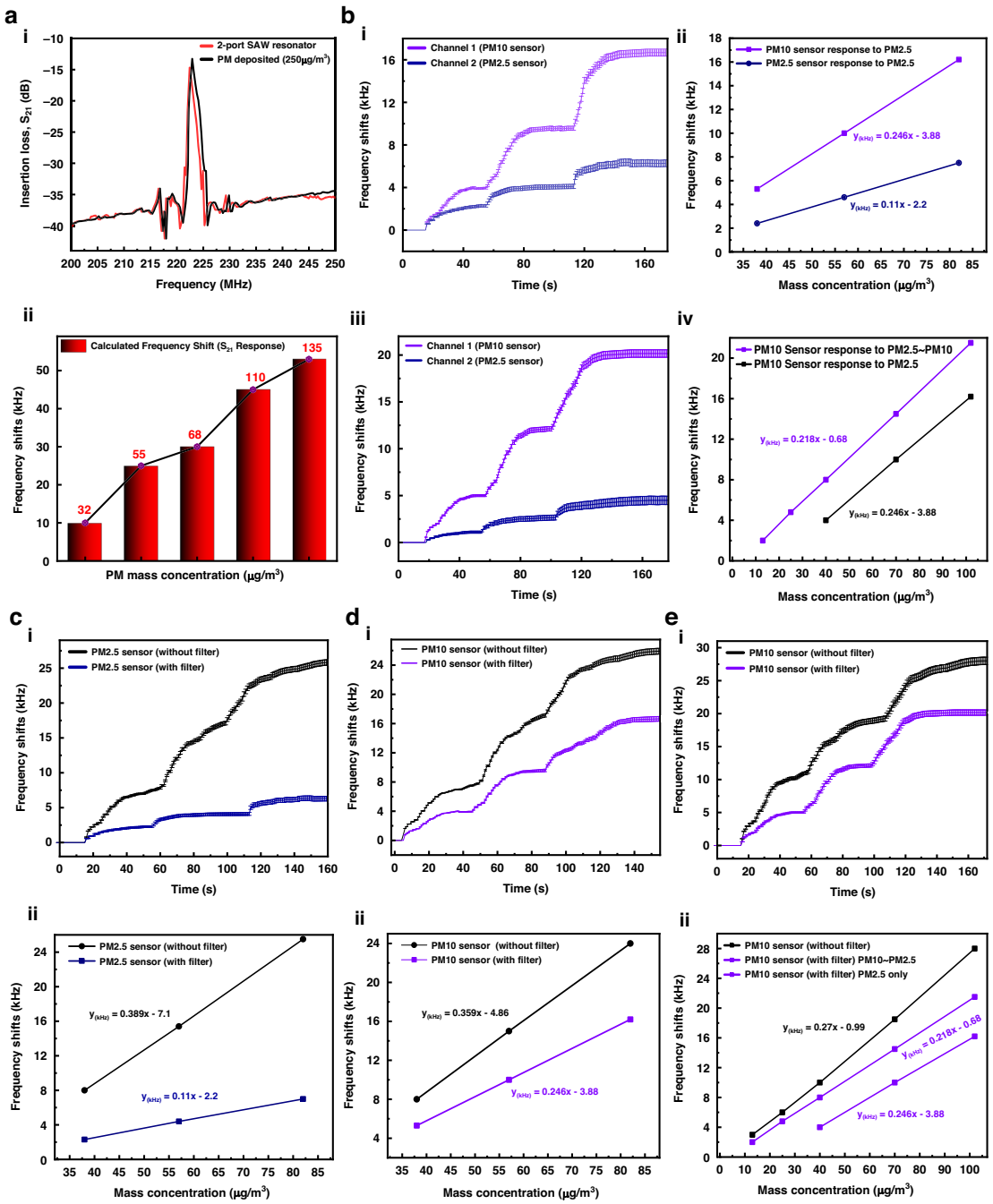

Fig. 4 Sensor characterization results using network analyzer and interface electronics. a S_{21} measurements of the fabricated two-port SAW resonator sensor. **i** frequency response before and after PM deposition (250 μg/m^2), showing insertion loss characteristics. **ii** extracted frequency shifts plotted against PM mass concentration**. b** PM2.5 and PM10 testing with interface electronics. **i** Frequency shift measurements of both sensors when exposed to PM2.5 particles. **ii** Calibration data for PM2.5 particles obtained from both PM2.5 and PM10 sensors. **iii** Frequency shift measurements of both sensors when exposed to PM10 particles. **iv** Calibration data for PM10 sensor, when PM10 and PM2.5 are tested. **c** PM2.5 sensor response measurements with and without filters. **i** Frequency shift response of the PM2.5 sensor when exposed to PM2.5 particles. **ii** Calibration curve for the PM2.5 sensor. **d** PM10 sensor response measurements with and without filters under PM2.5 exposure **i** frequency shift response of the PM10 sensor **ii** Calibration curve for the PM10 sensor under PM2.5 exposure. **e** PM10 sensor response measurements with and without filter under PM10 exposure **i** Frequency shift response of the PM10 sensor **ii** Calibration curve for the PM10 sensor under PM10 exposure

caused solely by particles in the PM2.5–PM10 size range. After applying the subtraction method to isolate the 2.5–10 μm fraction, the net sensitivity of the PM10 channel to particles in this size range was calculated to be 0.218 kHz/(μg/m^3). This correction allowed for accurate calibration of the sensor response corresponding to particles in the 2.5–10 μm range, as shown in Fig. 4biv. Thus, the developed sensor system is capable of providing real-time classification and information on PM mass concentration according to particle size ranges—PM2.5, PM2.5–PM10, and PM10.

Assessment of particle infiltration efficiency through a porous membrane

The particle infiltration efficiency, defined as the ability of particles to pass through the porous membrane, was quantitatively evaluated. Detailed calibration procedures used for this assessment are provided in the Supplementary Information. To perform the evaluation, two sets of sensors with identical specifications were prepared: one with a PM2.5 filter and one without, and similarly, one with a PM10 filter and one without. Each pair was tested using both PM2.5 and PM10 particles. For the PM2.5 sensor, known concentrations of PM2.5 particles were introduced into the test chamber, and frequency shifts were recorded for both the filtered and unfiltered sensors. At a particle concentration of 80 μg/m^3, the unfiltered sensor exhibited a frequency shift of ~25 kHz, while the sensor with the PM2.5 filter showed a reduced shift of around 6.77 kHz (Fig. 4ci). The comparison is plotted in the calibration curve shown in Fig. 4cii. This reduction in frequency shift is attributed to the PM2.5 filter design, which includes 2.5 μm-diameter holes surrounded by a blocked region. This configuration improves the mechanical stiffness and ductility of the membrane, but also limits particle penetration. Despite this, the sensor system still demonstrated reliable measurement performance, as evidenced by the consistent frequency shift behavior relative to particle concentration, confirming its capability to detect PM2.5 even with the filter in place. Similarly, for the PM10 sensor tested with PM2.5 particles, results are presented in Fig. 4di, with the corresponding calibration data shown in Fig. 4dii. Due to the larger open area in the PM10 filter, the filtered sensor exhibited a higher frequency shift than the PM2.5-filtered sensor under the same particle exposure, even though the sensor structures were otherwise identical. In the second test, the PM10 sensor was evaluated using known concentrations of PM10 particles (90 μg/m^3). The unfiltered sensor showed a frequency shift of approximately 30 kHz at saturation, while the filtered sensor reached a maximum shift of around 20 kHz (Fig. 4ei). To isolate the frequency response due to particles in the PM2.5–10 μm size range, the same subtraction-based calibration method described in Fig. 4biv was applied here and presented in Fig. 4eii. Although only a fraction of the airborne particles adheres directly to the sensor surface, the measured frequency shifts closely match the calibration curves, confirming the reliability and repeatability of the sensing system for both simultaneous and individual detection of PM2.5 and PM10.

Microheater experimental characterization and reusability of the device

Before conducting direct PM sensing, the performance of the integrated microheater was first evaluated through two experimental tests to ensure that the desired temperature was achieved when voltage was applied. The testing method is already explained in detail in our previous study[44]. In the first test, thermal distribution during microheater operation was captured using a FLIR C5 infrared camera, as shown in Fig. 5a. For accurate thermal measurement, the emissivity of the $LiNbO_3$ substrate ($\varepsilon = 0.4–0.45$)[45] was applied in the camera settings. As shown in Fig. 5ai, the temperature at the sensor surface in the cavity region reached approximately 98 °C. In Fig. 5aii, the thermal distribution is presented using a lower emissivity setting ($\varepsilon = 0.1–0.23$) for pt metal[46], confirming a maximum temperature rise of up to 95 °C. These measurements were conducted using multiple emissivity settings because the surface temperature detected by infrared imaging is highly sensitive to the emissivity input. Since different materials exhibit distinct emissivity characteristics, incorrect emissivity values can result in significant errors in temperature estimation. In the second test, the microheater's performance was assessed using a microprobe station (NEXTRON Co.) equipped with a temperature controller to apply heat inside a sealed test chamber. The setup included a temperature control unit and a power supply to regulate the sensor surface temperature via applied voltage. Resistance measurements were performed using a Keithley 2400 source meter in a four-probe configuration to ensure accuracy. Temperature control and data acquisition were automated using NEXTRON software. Using the temperature controller, heat was applied inside the chamber, and the resulting resistance of the temperature sensor was measured. Fig. 5bi shows that the temperature sensor's resistance increased stepwise with temperature increments from 30 °C to 160 °C on the surface. A calibration curve (Fig. 5bii) correlating resistance with temperature exhibited excellent linearity, with a sensitivity of 0.591 Ω/°C and $R^2 = 0.997$. As illustrated in Fig. 5biii, the resistance of the temperature sensor increased with applied voltage (1–12 V) to the microheater, indicating a rise in surface temperature due to Joule heating. Fig. 5biv confirms the relationship between the temperature sensor's resistance and the corresponding surface temperature, measured

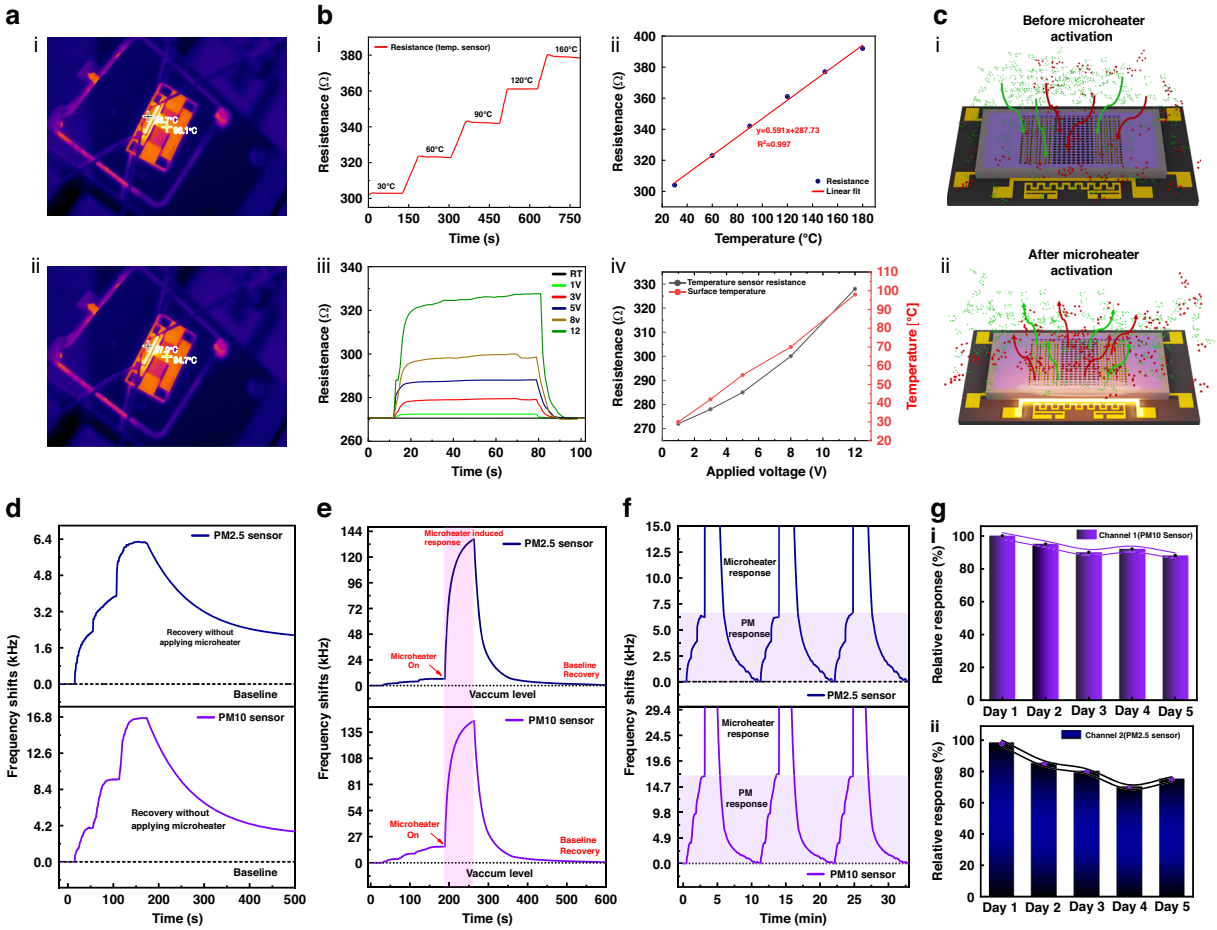

Fig. 5 Evaluation of microheater-assisted recovery performance in SAW PM sensors. a Temperature distribution across the sensor surface captured using a FLIR C5 thermal camera **i** emissivity set to 0.4 (for $LiNbO_3$ substrate). **ii** Emissivity setting applied for metal surfaces. **b** Microheater and temperature sensor evaluation using Nextron probe station result. **i** Resistance variation of the temperature sensor with ambient temperature changes. **ii** Calibration plot of temperature sensor resistance versus temperature. **iii** Temperature sensor resistance measured under different voltages applied to the microheater. **iv** Correlation between temperature sensor resistance and corresponding surface temperature under various applied microheater voltages. **c** Schematic illustrations showing the sensor surface condition. **i** particle attachment before microheater activation and **ii** particle removal after microheater activation. **d** Frequency shift response and natural recovery behavior of PM2.5 and PM10 sensors without microheater activation. **e** Enhanced recovery performance with microheater activation under vacuum conditions. **f** Repeatability test showing three consecutive PM exposure and recovery cycles facilitated by the integrated microheater. **g** Stability and reusability of the SAW-based PM sensors over five consecutive days. **i** The PM10 channel response. **ii** PM2.5 channel response, confirming effective microheater-assisted recovery

inside the chamber during voltage application to the microheater. The temperature reached ~100 °C at 12 V, demonstrating a fast and stable thermal response. The microheater exhibited consistent performance with minimal delay, consuming ~2.5 W at 12 V.

During PM testing, particles pass through the filter and adhere to the sensor surface, causing saturated frequency shifts and limiting sensor reusability due to incomplete baseline recovery. To overcome this, an on-chip microheater was integrated into the SAW sensor for active desorption and extended lifespan. The mechanisms of particle adhesion and thermally induced detachment are illustrated in Fig. 5c(i, ii). After three PM exposure cycles, vacuum induced only partial signal recovery, with the sensor failing to return to baseline (Fig. 5d), indicating persistent particle adhesion at room temperature. Activating the microheater at approximately 12 V raised the surface temperature to around 100 °C, based on pre-established calibration data. This temperature was selected to enable the detachment of particles adhered to the sensor and porous membrane surfaces, without altering the piezoelectric properties of the substrate. Since the LN substrate has a temperature coefficient of delay (TCD) of 75 ppm/°C, activation of the microheater caused heating of the substrate, leading to an additional frequency shift (Fig. 5e). After reaching the setpoint temperature, the

microheater voltage was turned off, allowing the sensors to cool naturally. The elevated temperature significantly accelerated particle desorption, enabling rapid and repeatable baseline recovery to the initial level, as shown in Fig. 5e. This thermally assisted recovery was validated over three repeated cycles, each demonstrating near-complete restoration (Fig. 5f), with minor deviations (2–4%) attributed to residual heat during the cooling phase. To clearly illustrate the recovery behavior of the sensors, frequency shifts caused by substrate heating beyond a certain threshold were intentionally omitted, and the repeated three-cycle data are presented in Fig. 5f. The stability tests over five consecutive days simultaneously validated both the porous microstructure filter and the integrated microheater. As shown in Fig. 5gi, the PM10 channel maintained more than 90% of its relative response, while the PM2.5 channel retained above 80% with only minor fluctuations (Fig. 5gii). Although the PM2.5 channel response decreased slightly below 80% on the fifth day, this can be attributed to several factors: (i) the 3 μm pores of the PM2.5 filter are more susceptible to partial clogging by borderline particles (>3 μm) that may occasionally enter and adhere, (ii) smaller pore size increases the likelihood of temporary surface fouling, which may slightly reduce airflow and effective particle infiltration, and (iii) accumulated residues at the pore edges require more complete regeneration, making the PM2.5 channel more sensitive to minor variations in microheater efficiency. These results demonstrate that the filter pores consistently enabled size-selective particle capture during repeated measurement–recovery cycles. At the same time, the repeated operation confirmed that larger particles did not block the microheater region or hinder its detachment function, as the device reliably recovered to baseline levels after each cycle. The slight variation observed is attributed to differences in particle loading and detachment efficiency; however, the overall reproducibility highlights the robustness of both the filter design and the microheater-assisted recovery process.

Comparison with other sensors

Table 1 presents a state-of-the-art comparison with previously reported studies on SAW-based PM sensors. Most prior sensors have focused on detecting a single particle size and primarily relied on simple single-particle attachment mechanisms. These reported systems typically employed external separation components (e.g., cyclones or impactors) and were generally limited to single-use operation. In contrast, our study introduces a SAW sensor integrated with a porous microstructured filter membrane, enabling simultaneous and size-selective detection of both PM2.5 and PM10. This integrated approach eliminates the need for external separation hardware, resulting in a more compact and scalable sensing platform. Notably, this work demonstrates the first implementation of a reusable SAW-based PM sensor, achieved through the integration of a microheater. Together, these features contribute to a robust, reusable, and practical system for real-time, multi-size particulate matter monitoring.

Built-in environmental effect compensation using interface electronics

The $LiNbO_3$ substrate is sensitive to environmental factors, such as temperature and vibration, requiring compensation to ensure accurate sensor measurements. To evaluate the effectiveness of compensation, tests were conducted under varying temperature conditions. For temperature compensation, the system was subjected to a gradual increase in temperature from room temperature to 90 °C (Fig. S3). When using a signal generator as the reference, the frequency shifts showed significant deviations, reaching up to 800 kHz as the temperature increased. This highlights the inability of the signal generator to account for temperature-induced variations. However, when employing a SAW reference device identical to the sensing device, the frequency shift caused by ambient temperature variations was reduced to negligible levels, with deviations remaining minimal across the entire tested temperature range. This demonstrates that the SAW reference device effectively compensates for temperature fluctuations by experiencing and canceling out the same thermal effects as the sensing device.

Conclusion

In this study, we successfully developed a multichannel SAW-based PM sensor system for the simultaneous and individual detection of PM10 and PM2.5 with high sensitivity and reusability for the first time. Experimental validation demonstrated that the mechanical filter membrane effectively separated PM10 and PM2.5. Additionally, compared to conventional SAW-based PM sensors, which only facilitate PM particle attachment for sensing, our sensor system also offers reusability through the integration of a microheater for effective particle detachment. The microheater efficiently restored the sensor to baseline levels after PM exposure, achieving a maximum temperature of ~100 °C under vacuum conditions. Furthermore, since both sensors were exposed to the same environment, a detailed calibration study was conducted to ensure the separate detection of PM10 and PM2.5. Our system is capable of providing real-time data on the percentage of PM2.5 and PM10 present in the air, utilizing the calibration data for accurate quantification. Overall, this study presents a significant advancement in SAW-based PM sensing technology, offering a scalable, reusable, and highly sensitive solution for air quality monitoring applications.

Table 1 Summary of related work and performance metrics

Device	Operating frequency (MHz)	Separation method	Target PM size	Q factor	Sensitivity (Hz/min μg/m^3)	Calibration method	Response time(s)	Detection limit (μg/m^3)	Sensor reusability
QCM[47]	5	3D-printed virtual impactor	PM2.5	_	0.0554	NaCl evaporation	>60	~10–20	No
SAW[37] Device	180.4	_	PM2.5	853	~78.33	Commercial PM sensor	30	~1	No
SAW[48] device	147.24	3D-printed virtual impactor	PM 1	_	7.446	NaCl evaporation	~5–10	~5	No
SAW[21] device	122	Cyclone (microcentrifuge tube)	PM 2.5	_	2.25	Commercial monitor	160	11	No
SAW[27] device	125	Cascade impactor	PM10 & PM2.5	_	_	Optical counter	~60	1	No
Dual SAWR[32]	262	_	PM 2.5	1000	275	Particle deposition	~40–60	<1 ng	No
SAWR device[49]	311	Cascade impactor	PM10 & PM2.5	_	_	Cascade, PSL calibration	~45	_	No
QCM[50]	10	_	PM10, PM2.5, PM1	_	_	NaCl aerosol + OPC reference monitor	~60	~15	No
This work	222.52	Porous microstructured membrane	PM10 & PM2.5	890	~93.45	NaCl solution & PM dust	~30	1	Yes microheater

All sensitivities mentioned in the table were recalculated and normalized to Hz per minute per μg/m^3 for consistent comparison

Materials and methods

Sensor fabrication

A 4-inch 128° YX-cut $LiNbO_3$ substrate was sequentially cleaned with acetone, isopropyl alcohol (IPA), and deionized (DI) water to remove organic residues. DNR-L300 negative photoresist (PR) was spin-coated to form an approximately 3 μm-thick film, followed by a soft bake at 90 °C for 90 s. UV exposure was carried out using a chrome mask patterned with the optimized layout of the two-port SAW resonator and integrated microheater, at an intensity of 13.4 mW for approximately 15 s. A hard bake at 110 °C for 90 s was then performed to enhance photoresist stability. The exposed PR was developed in AZ 300 MIF for 30 s. Subsequently, a Ti/Pt (10/100 nm) metal layer was deposited using an electron-beam evaporator, and a lift-off process was employed to define the SAW resonator, microheater, and temperature sensor structures. The microheater and temperature sensor were positioned near the cavity of the two-port SAW resonator for localized thermal control and monitoring. Finally, the wafer was diced into individual sensor devices. The complete sensor fabrication process is also illustrated in Fig. 1c (left).

Porous microstructure filter membrane fabrication

A 4 μm-thick layer of GXR 601 photoresist is spin-coated onto a silicon (Si) substrate comprising a 0.3 μm SiO_2 layer, a 20 nm chromium (Cr) layer, and a 200 nm gold (Au) layer, both deposited via electron beam evaporator. The coated substrate undergoes UV exposure through a photomask, altering the photoresist's chemical properties in exposed regions. Subsequent development removes these areas, revealing the underlying Au layer. Gold wet etching is performed using a solution of nitric acid, hydrochloric acid, and DI water (1:2:1) for 25 seconds, followed by chromium etching with diammonium hexanitratocerate and nitric acid for 40 seconds. The remaining photoresist is lifted off using acetone in 7 seconds. Nickel (Ni) was then electroplated onto the exposed areas using a nickel sulfate ($NiSO_4$) electrolyte. A nickel plate served as the counter electrode. The electrolyte concentration was optimized to 0.1 M, with a deposition time of 25 minutes and a current density of 2 mA/cm^2 to achieve a uniform and smooth surface. The solution temperature was carefully maintained between 50 °C and 60 °C to ensure consistent deposition across the non-planar surface containing multiple microscale holes. The pH of the electrolyte was maintained below 4 to support stable and controlled deposition. These optimized conditions enabled uniform Ni deposition with improved coverage and surface quality. After that, the SiO_2 layer is etched with buffered oxide etchant for 24 hours to fully separate the nickel structures. Subsequently, a thick gold layer was deposited onto the ductile metal membrane using a coater to provide a hydrophobic, inert, and corrosion-resistant surface. Finally, the microstructured membrane filters were assembled onto a 3D-printed frame with dimensions of 5 mm × 6 mm × 1 mm, specifically designed to precisely cover the sensor area, allowing particle passage only through the filter holes positioned directly above. The frame was carefully engineered to support the filter membrane without inducing degassing, minimizing internal volume, and avoiding interference with SAW propagation. This design enables rapid concentration equilibrium with the external environment, thereby completing the fabrication process. For improved clarity and visualization, all fabrication steps are illustrated in Fig. S2.

Fine dust preparation

Commercial standard fine dust samples of PM10 and PM2.5 were purchased from Sigma-Aldrich (Merck Life Science, South Korea). The PM10 (aerodynamic diameter ≤10 μm) and PM2.5 (≤2.5 μm) powders were used as received without further purification. PM10 standard: [Fine dust PM10-like], PM2.5 standard: [Fine dust PM2.5], Sigma-Aldrich, Cat. No. [ERM-CZ120], sample No.1844.

Reference commercial PM sensor

For reference measurements, a portable real-time particulate matter monitor (MSMS-S4, Shanghai XuanHan Electronics Technology Co., Ltd.) was employed, capable of simultaneously detecting PM1.0, PM2.5, and PM10 mass concentrations. The device operates on a light-scattering optical principle using an internal laser-based sensor and reports concentrations in $\mu g/m^3$. Key specifications include a measurement range of 0–500 $\mu g/m^3$, resolution of 1 $\mu g/m^3$, accuracy of ±10 $\mu g/m^3$ or ±10% of the reading, and a response time of ~10 s. The monitor features a 3.0-inch LCD display, compact dimensions (112 × 46 × 65 mm) with a weight of ~200 g, and is powered by a 3250 mAh rechargeable battery supporting continuous operation.

Acknowledgements

This research was funded by the Ministry of Science and ICT (RS-2023-00278288, RS-2024-00457846, and RS2023-NR119846).

Author contributions

F.N.: conceptualization, methodology, data curation, formal analysis, measurement, validation, writing—original draft; N.T.: formal analysis; K. Lee.: conceptualization, methodology, resources, writing—review & editing, supervision, project administration, funding acquisition. All authors contributed through scientific discussions.

Competing interests

The authors declare no competing interests.

Ethics approval and consent to participate
Not applicable.

Supplementary information The online version contains supplementary material available at https://doi.org/10.1038/s41378-025-01137-5.

Received: 11 June 2025 Revised: 3 November 2025 Accepted: 29 November 2025
Published online: 24 March 2026

References

1. Bowe, B., Xie, Y., Yan, Y. & Al-Aly, Z. Burden of cause-specific mortality associated with PM $_{2.5}$ air pollution in the United States. *JAMA Netw. Open* **2**, e1915834 (2019).
2. Sang, S., Chu, C., Zhang, T., Chen, H. & Yang, X. The global burden of disease attributable to ambient fine particulate matter in 204 countries and territories, 1990–2019: a systematic analysis of the global burden of disease study 2019. *Ecotoxicol. Environ. Saf.* **238**, 113588 (2022).
3. Schraufnagel, D. E. et al. Air pollution and noncommunicable diseases. *Chest* **155**, 409–416 (2019).
4. Kampa, M. & Castanas, E. Human health effects of air pollution. *Environ. Pollut.* **151**, 362–367 (2008).
5. Dockery, D. W. & Pope, C. A. Acute respiratory effects of particulate air pollution. *Annu. Rev. Public Health* **15**, 107–132 (1994).
6. Chen, R. et al. Beyond PM2.5: the role of ultrafine particles on adverse health effects of air pollution. *Biochim. Biophys. Acta.* **1860**, 2844–2855 (2016).
7. West, J. J. et al. Co-benefits of mitigating global greenhouse gas emissions for future air quality and human health. *Nat. Clim. Chang* **3**, 885–889 (2013).
8. Burnett, R. T. et al. An integrated risk function for estimating the global burden of disease attributable to ambient fine particulate matter exposure. *Environ. Health Perspect.* **122**, 397–403 (2014).
9. Zhu, C., Maharajan, K., Liu, K. & Zhang, Y. Role of atmospheric particulate matter exposure in COVID-19 and other health risks in human: a review. *Environ. Res* **198**, 111281 (2021).
10. Dominici, F. et al. Fine particulate air pollution and hospital admission for cardiovascular and respiratory diseases. *JAMA.* **295**, 1127 (2006).
11. Pope, C. A., Ezzati, M. & Dockery, D. W. Fine-particulate air pollution and life expectancy in the United states. *N. Engl. J. Med.* **360**, 376–386 (2009).
12. Zhang, N., Zhang, A., Wang, L. & Nie, P. Fine particulate matter and body weight status among older adults in China: Impacts and pathways. *Health Place* **69**, 102571 (2021).
13. Wu, X., Nethery, R. C., Sabath, M. B., Braun, D. & Dominici, F. Air pollution and COVID-19 mortality in the United States: Strengths and limitations of an ecological regression analysis. *Sci. Adv.* **6**, eabd4049 (2020).
14. Shukla, K. & Aggarwal, S. G. A Technical overview on beta-attenuation method for the monitoring of particulate MATTER IN AMBIENT Air. *Aerosol Air Qual. Res* **22**, 220195 (2022).
15. Chow, J. C. Measurement methods to determine compliance with ambient air quality standards for suspended particles. *J. Air Waste Manag. Assoc.* **45**, 320–382 (1995).
16. Jobert, G. et al. Miniature particulate matter counter and analyzer based on lens-free imaging of light scattering signatures with a holed image sensor. *Sens. Actuators Rep.* **2**, 100010 (2020).
17. Takahashi, K., Minoura, H. & Sakamoto, K. Examination of discrepancies between beta-attenuation and gravimetric methods for the monitoring of particulate matter. *Atmos. Environ.* **42**, 5232–5240 (2008).
18. Trebs, I., Lett, C., Krein, A., Matsumoto Kawaguchi, E. & Junk, J. Performance evaluation of an online monitor based on X-ray fluorescence for detecting elemental concentrations in ambient particulate matter. *Atmos. Meas. Tech.* **17**, 6791–6805 (2024).
19. Korevaar, M., Ogink, N. & Winkel, A. Evaluation of a gravimetrical method with a cyclonic pre-separator against the reference method for measuring high PM10 mass concentrations in livestock houses. *Atmos. Environ.* **346**, 121076 (2025).
20. Steiner, D. & Lanzerstorfer, C. Particulate emissions from biomass power plants: a practical review and measurement uncertainty issues. *Clean. Technol. Environ. Policy* **26**, 1039–1048 (2024).
21. Kuo, F.-Y., Lin, Y.-C., Ke, L.-Y., Tsai, C.-J. & Yao, D.-J. Detection of particulate matter of size 2.5 μm with a surface-acoustic-wave sensor combined with a cyclone separator. *Micromachines* **9**, 398 (2018).
22. Kim, H., Kim, J. & Roh, S. Effects of gas and steam humidity on particulate matter measurements obtained using light-scattering. *Sens. Sens.* **23**, 6199 (2023).
23. Zeng, J. et al. On-line high-accuracy particulate matter monitoring technology using multi-channel scattering signals. *Opt. Express* **29**, 41343 (2021).
24. Eckenberger, E. et al. Performance evaluation of four cascade impactors for airborne ultrafine-particle (UFP) collection: the influence of particle type, concentration, mass, and chemical nature. *Aerosol. Res.* **3**, 45–64 (2025).
25. Rivera-García, M. O. et al. Cyclone separator for air particulate matter personal monitoring: a patent review. *Atmosphere* **14**, 624 (2023).
26. Seok, J., Chun, K. M., Song, S. & Lee, S. Study on the filtration behavior of a metal fiber filter as a function of filter pore size and fiber diameter. *J. Aerosol Sci.* **81**, 47–61 (2015).
27. Djoumi, L., Vanotti, M. & Blondeau-Patissier, V. Real time cascade impactor based on surface acoustic wave delay lines for PM10 and PM2.5 mass concentration measurement. *Sensors* **18**, 255 (2018).
28. Song, C. et al. Numerical analysis of forces exerted on particles in cyclone separators. *Powder Technol.* **294**, 437–448 (2016).
29. Liu, X., Shen, H. & Nie, X. Study on the filtration performance of the baghouse filters for ultra-low emission as a function of filter pore size and fiber diameter. *Int. J. Environ. Res. Public Health* **16**, 247 (2019).
30. Liu, J., Hao, W., Liu, M., Liang, Y. & He, S. A novel particulate matter 2.5 sensor based on surface acoustic wave technology. *Appl. Sci.* **8**, 82 (2018).
31. Yang, J. & Lu, J. Study of size-related sensitivity of surface acoustic wave sensor towards particulate matter sized particles using finite element and experimental methods. *AIP Adv.* **10**, 025324 (2020).
32. Thomas, S., Racz, Z., Cole, M. & Gardner, J. W. Dual high-frequency surface acoustic wave resonator for ultrafine particle sensing. In *2013 IEEE SENSOR0S* 1–4 (IEEE, 2013). https://doi.org/10.1109/ICSENS.2013.6688319.
33. Thomas, S., Cole, M., Villa-López, F. H. & Gardner, J. W. High frequency surface acoustic wave resonator-based sensor for particulate matter detection. *Sens Actuators A Phys.* **244**, 138–145 (2016).
34. Lin, Q., Zhao, C., Li, M. & Xu, H. Recent progress in surface acoustic wave sensors based on low-dimensional materials and their applications. *Chemosensors* **12**, 255 (2024).
35. Segura Chávez, P. et al. Love wave sensor with high penetration depth for potential application in cell monitoring. *Biosensing* **12**, 61 (2022).
36. Dbibih, F.-E. et al. Measurement of PM10 and PM2.5 using SAW sensors-based Rayleigh wave and love wave. In *The 8th International Symposium on Sensor Science* 81 (MDPI, Basel Switzerland, 2021). https://doi.org/10.3390/I3S2021Dresden-10129.
37. Singh, G., Kim, S. & Lee, K. Development of a highly sensitive and portable particulate matter SAW sensor and interface electronics. *Sens Actuators A Phys.* **343**, 113641 (2022).
38. Fahim, F., Mainuddin, M., Mittal, U., Kumar, J. & Nimal, A. T. Novel SAW CWA detector using temperature programmed desorption. *IEEE Sens J.* **21**, 5914–5922 (2021).
39. Aleksandrova, M. et al. Microheater topology for advanced gas sensor applications with carbyne-enriched nanomaterials. *Appl. Sci.* **14**, 1728 (2024).
40. de Jong, A. M. & Niemantsverdriet, J. W. Thermal desorption analysis: comparative test of ten commonly applied procedures. *Surf. Sci.* **233**, 355–365 (1990).
41. Nawaz, F. et al. Toward ultrafast response and recovery characteristics through ZnO multilayer thin films in surface acoustic wave UV sensor. *IEEE Sens J.* **25**, 343–353 (2025).
42. Kim, S. et al. Development of highly sensitive and solar blind surface acoustic wave UV-C photodetector based on the In2O3/Ta2O5 nano-heterojunction and its interface electronics. *Sens Actuators A Phys.* **367**, 115027 (2024).
43. Kim, S., Nawaz, F., Choi, C., Jeon, I. & Lee, K. Synthesis and characterization of high-quality Ta $_2$ O $_5$ nanoparticles for highly selective SAW-based DUV sensor and corona detection application. *Adv. Mater. Technol.* **9**, 2301486 (2024).
44. Nawaz, F., Lee, H., Wang, W. & Lee, K. Development of ultra-fast surface acoustic wave-based NO2 sensor incorporating a monolayered graphene: MoS2 Sensing material and a microheater for spacecraft applications. *Appl. Sci.* **15**, 4050 (2025).

45. Salas, O., Garcés, E., Castillo, F. L. & Magaña, L. F. Absorption and reflectivity of the lithium niobate surface masked with a graphene layer. *AIP Adv.* **7**, 015305 (2017).
46. Madjid, A. H., Stover, R. L., Martinez, J. M. & Grimvall, G. Normal spectral emissivity of platinum in the red and in the green in vacuum and helium. *Phys. Condens. Matter* **17**, 125–134 (1974).
47. Wang, Y. et al. A miniature system for separation and detection of PM based on 3-D printed virtual impactor and QCM sensor. *IEEE Sens J.* **18**, 6130–6137 (2018).
48. Wang, Y. et al. An aerosol sensor for PM1 concentration detection based on 3D printed virtual impactor and SAW sensor. *Sens Actuators A Phys.* **288**, 67–74 (2019).
49. Chen, Z., Liu, J., Liu, M., You, R. & He, S. An aerosol sensor for multi-sized particles detection based on surface acoustic wave resonator and cascade impactor. *Appl. Sci.* **11**, 9833 (2021).
50. Zampetti, E. et al. Exploitation of an integrated microheater on QCM sensor in particulate matter measurements. *Sens Actuators A Phys.* **264**, 205–211 (2017).